International Journal of Heat and Mass Transfer 52 (2009) 5731–5739

Contents lists available at ScienceDirect

International Journal of Heat and Mass Transfer

journal homepage: www.elsevier.com/locate/ijhmt

Analysis of vapor–gas bubbles in a single artery heat pipe

Tarik Kaya

Carleton University, Department of Mechanical and Aerospace Engineering, 1125 Colonel By Drive, Ottawa, Ont., Canada K1S 5B6

ARTICLE INFO

Article history:
Received 19 March 2009
Received in revised form 19 August 2009
Available online 19 September 2009

Keywords:
Heat pipes
Arterial heat pipes
Meniscus coalescence
Vapor–gas bubbles

ABSTRACT

The noncondensable gas supported bubbles in an arterial heat pipe are studied. The governing conservation equations are solved to study the growth/collapse of spherical bubbles under different conditions by using the finite element method. The criterion used in the design of the venting pores to prime the artery is explained. The diffusion-limited bubble collapse in the condenser and bubble growth due to the phase change in the evaporator are both studied. A theoretical explanation for the capability of venting bubbles under different scenarios is provided. The experimental results, including rapid startup and condenser cooldown, are also presented to prove the ability of the heat pipes to vent vapor–gas bubbles.

1. Introduction

A heat pipe is a passive, reliable and highly efficient heat transfer device operating on a continuous evaporation–condensation cycle of a working fluid driven by capillary forces. Since the first patent in 1944 [1], and more particularly the subsequent work performed by Grover et al. [2], heat pipes have been extensively studied and different types have been introduced to satisfy various mission requirements. Currently, heat pipes are widely used as standard thermal control hardware in space and ground applications. A typical heat pipe consists of a sealed container with a capillary structure filled with an appropriate working fluid. The capillary structures used in heat pipes include screen mesh, sintered metal powder, axial grooves, arteries and suitable combination of these structures. The heat transferred by a heat pipe is mainly limited by the available capillary pressure. It is possible to increase the capillary pressure by increasing the effective meniscus curvature of the capillary structure, for example using a smaller pore size for a sintered wick. However, this lowers the permeability of the capillary structure, leading to higher viscous pressure losses within the capillary structure. Several design solutions have been proposed to improve the heat transfer limit by optimizing these two competing parameters. In the 1970s, arterial heat pipes (AHP) were introduced to minimize viscous losses by using separate fluid flow passages or arteries in combination with fine capillary structures.

Although several AHP designs have been proposed in the past, many of these developments were mostly abandoned as a result of failures during the ground and space flight experiments. The main difficulty was their susceptibility to the blockage due to the presence of vapor or noncondensable gases (NCG) in the liquid artery, leading to startup failures or dryout. The most important of these designs are reviewed later in this section.

In this work, an innovative artery design was considered. The AHP configuration studied, shown in Fig. 1, was developed by Goncharov et al. [3] in Russia based on an earlier design by Blinchevskii et al. [4]. This AHP is made of a stainless steel tube with a wall thickness of 0.5 mm. A single artery is formed using a stainless steel mesh of 680 wires per inch by contact spot welding. The mesh thickness is 0.12 mm. Circumferential screw grooves on the inside wall are arranged along the entire length. The height and width of the artery are 1.5 and 7.63 mm, and the depth and width of the circumferential grooves are 0.15 and 0.1 mm, respectively. The circumferential grooves provide the additional capillary structure for liquid transportation from the liquid artery along the circumference of the heat pipe. They also provide a large uniform thin film for evaporation, which helps prevent boiling in the liquid artery. The remaining section of the heat pipe envelope is reserved for the vapor flow. As a result, the liquid and vapor flow is separated and the entrainment constraint due to the liquid–vapor countercurrent flow is eliminated.

A common problem encountered in similar artery designs was the glazing effect: the fine mesh wick which forms the artery wets more rapidly than the artery can self-prime (filled with liquid), leading to vapor blockage in the artery. A solution to the glazing effect was the meniscus coalescence technique, first proposed by Eninger [5]. A sufficiently thin foil with very small venting pores ensures that the menisci on opposite sides of the liquid in this venting pore coalesce to keep the pore open. In [5], an analytical solution was provided to calculate the priming foil thickness and venting hole diameter as a function of the liquid–vapor pressure difference. Starting from this equation, the venting hole diameter

---

E-mail address: tkaya@mae.carleton.ca

0017-9310/$ - see front matter © 2009 Elsevier Ltd. All rights reserved.
doi:10.1016/j.ijheatmasstransfer.2009.08.015

Nomenclature

c_p	specific heat at constant pressure (J kg^{-1} K^{-1})
c_β	solvent molar concentration (kmol m^{-3})
D_p	venting pore diameter (m)
$D_{\alpha\beta}$	mass diffusivity (m^2 s^{-1})
fx	mole fraction of the NCG species dissolved in the liquid
fy	mole fraction of species in the NCG
h	artery height (m)
h_{fg}	latent heat of evaporation (J kg^{-1})
J_α	molar flux of species α (kmol m^{-2} s^{-1})
k	thermal conductivity (W m^{-1} K^{-1})
k_H	Henry's law constant (atm)
N	number of moles
P	pressure (Pa)
R	bubble radius (m)
r	radial coordinate (m)
R^*	universal gas constant (kJ kmol^{-1} K^{-1})
R_a	artery radius (m)
R_m	fillet radius (m)
T	temperature (K)
t	time (s)
u	velocity (m s^{-1})
x	solute mole fraction in the liquid phase
y	solute mole fraction in the vapor phase

Greek symbols

α	solute species
β	viscosity (Pa s)
θ	wetting angle (rad)
ρ	density (kg m^{-3})
σ	liquid–vapor surface tension (N m^{-1})
τ	artery mesh thickness (m)

Subscripts

c	condenser, critical
e	evaporator
i	initial
ℓ	liquid
sat	saturation
v	vapor

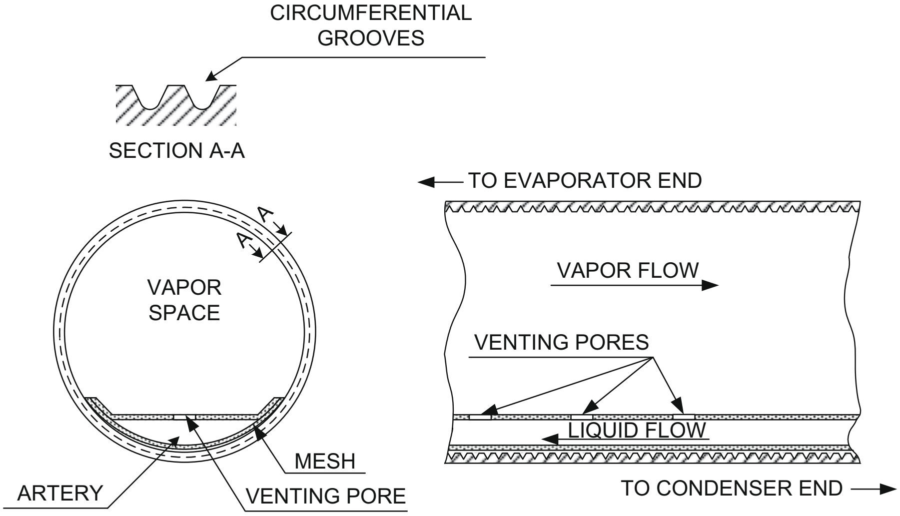

Fig. 1. Cross-section of the arterial heat pipe (not-to-scale).

was calculated by assuming the limiting liquid–vapor pressure difference required for priming the artery as the venting criterion, which leads to the following relation

$$D_p \geqslant \sqrt{\frac{\tau h}{\cos\theta}\left(2 - \frac{\tau\cos\theta}{h}\right)} \tag{1}$$

The venting hole size determines the maximum capillary pressure that the artery can support. Therefore, there is a trade-off in choosing the pore diameter. In [5], a separate priming foil was introduced into the screen mesh. In the AHP presented in this work, a single row of closely-spaced vapor vent holes with a radius of 0.254 mm were directly positioned on the mesh along the liquid artery, as shown in Fig. 1. These pores were limited to the evaporator section exclusively.

The most noteworthy designs among the earliest AHPs were the pedestal and spiral artery as shown in Fig. 2(a) and (b). These configurations were flown on the Orbital Astronomical Observatory (OAO-C) spacecraft [6]. The pedestal AHP had a circular cross-section artery with two retainer legs fabricated from stainless steel mesh. The artery was connected to the pipe wall by these two legs and the heat pipe envelope was aluminum tubing with circumferential screw grooves on the inside surface. The spiral AHP was also manufactured from aluminum tubing with internal circumferential grooves. The artery was formed by rolling a stainless steel screen mesh with successive gaps around a central rod. The formed spiral artery was connected to the pipe inside wall by a three-legged retainer again fabricated by stainless steel screen. Both pipes used ammonia. The pedestal artery design was difficult to prime because of its sensitivity to the gas bubble presence in the arteries; therefore, it had to be overcharged to induce priming in a 1-g environment. The spiral artery design was self-priming. However, because of the low vapor/liquid volume ratio, it was susceptible to condenser blockage by NCG or excess liquid. Therefore, its charge had to be accurate and the NCG tolerance was low.

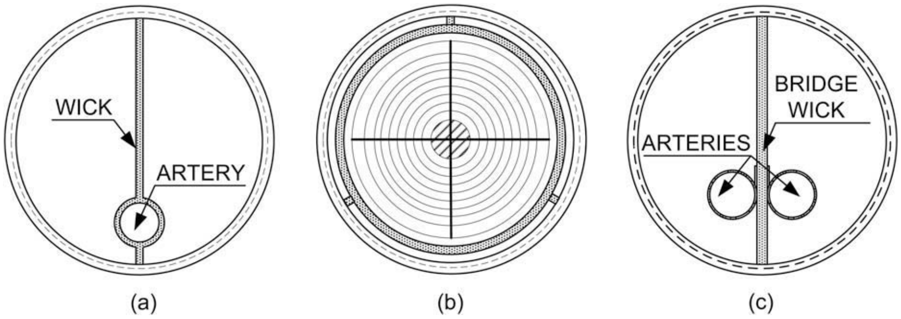

Fig. 2. Different arterial heat pipe designs (a) pedestal (b) spiral (c) CTS.

Another important AHP development work was undertaken to cool the traveling wave tube amplifiers aboard the Communication Technology Satellite (CTS) [7]. These AHPs had two circular cross-section arteries fabricated from stainless steel mesh as shown in Fig. 2(c). These two arteries were spot welded to a felt-metal bridge wick, which allows the liquid supply to the circumferential wall grooves from the arteries. A separate priming foil as suggested in [5] was incorporated into the evaporator section of the artery. The CTS pipes used methanol as the working fluid. The CTS AHPs suffered from occasional deprimes in orbit. Although the reason for deprimes was identified, this design was not used in the later missions.

It is beyond the scope of this paper to review all the AHP developments. A summary of additional AHP designs can be found in [8].

2. Problem statement

As it was stated earlier, the arterial blockage due to the NCG-supported bubbles has been a significant problem for AHPs. NCGs are either inevitably present during the manufacturing process or generated during the heat pipe operation as a result of chemical reactions. NCGs may also be intentionally introduced to control the heat pipe thermal conductance. Therefore, it is almost impossible to eliminate the NCG in a heat pipe. Once an NCG-supported bubble is formed in the arterial liquid, the bubble collapse is mainly governed by diffusion process. It was demonstrated that the dissolution time of a bubble can take a long time from many hours to days [9,10]. Then, bubbles may be convected to the evaporator where they can quickly swell because of the arterial superheat provided by the heat input. If the bubble becomes sufficiently large due to merging of smaller bubbles before reaching the evaporator, it may partially or fully block the artery, leading to low permeability or full arterial deprime. In this case, the bubble continues to grow into an elongated bubble until it reaches the evaporator.

Five different mechanisms for the appearance of NCG-supported bubbles in the artery were identified, which was used as the basis of the numerical and experimental investigation in this study: (1) During the freezing of the working fluid, NCG in the vapor space is dissolved into the arterial liquid and then form NCG pockets in the frozen solid. As the solid thaws, NCG-supported bubbles are discharged into the liquid [10]. (2) When a large heat load is suddenly applied to the pipe, NCG will be pushed to the end of condenser and the NCG partial pressure above the arterial liquid will decrease. As result, NCG dissolved in the liquid will come out of solution, forming bubbles in the condenser artery [11]. Similarly, under a rapid increase in power, the bubble formation by boiling may occur where the artery connects to the wall since the liquid here may be superheated with respect to the bulk liquid within the artery. (3) If the condenser temperature drops suddenly, the arterial liquid may become superheated because of the large difference in thermal capacitances between the liquid in the artery and circumferential wall grooves. If the superheat becomes sufficiently large, the resulting flash boiling process may form NCG-supported bubbles [11]. (4) The acceleration forces during the launch and other spacecraft maneuvers prior to startup may result in bubble formation as well as excessive elevation. (5) If the heat pipe goes through shutdown/restart cycles in the microgravity environment, there is a chance that bubbles may appear in the arteries.

The main objective of this work was to study the behavior of NCG-supported bubbles in a unique heat pipe design. Two different heat pipes using the same arterial design were considered: a variable conductance AHP (VCAHP) and a constant conductance AHP (CCAHP). A numerical model was developed to study the NCG-supported bubbles. The mathematical model was based on the past work presented in [10], where only the mass diffusion equation was considered. In our work, the momentum and energy equations were also taken into account. The ammonia–nitrogen–hydrogen system was considered. In the related past works, this fluid combination was not studied. The intentionally introduced NCG into the VCAHP to control the conductance brings an additional challenge: There is an increasing risk of bubble formation in the arteries due to the tendency of diffusion of the control gas into arterial liquid. The latter problem was numerically investigated. An experimental investigation was also undertaken to demonstrate the robustness of the arterial design under different bubble formation scenarios.

3. Formulation of governing equations

To study the growth/collapse rate of bubbles in the arteries, a one-dimensional spherical bubble model was developed. The bubble growth/collapse is governed by the gradients immediately near to the bubble interface. The effect of the geometrical constraints away from the interface is therefore secondary. As a result, the segmented artery, shown in Fig. 1, was represented by a circular cross

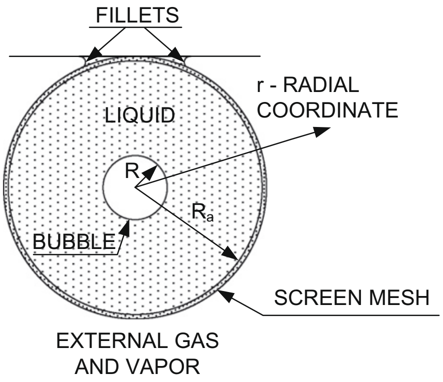

Fig. 3. Mathematical model geometry (not-to-scale).

section with the corresponding hydraulic radius of 0.98 mm. The model geometry is shown in Fig. 3. A spherical bubble consisting of the ammonia vapor and NCG with a given diameter was assumed to form in the artery as a result of one of the five mechanisms discussed above.

The major assumptions made in this work were: (1) The bubble will remain spherical during the growth/collapse. (2) The solution is dilute. (3) The diffusivity of a component into the solvent is not affected by the other dilute species in the solution. Under these assumptions, the equation of continuity for a multicomponent mixture in molar quantities and spherical coordinates with respect to the center of the bubble can be written as

$$\frac{\partial x_\alpha}{\partial t} + u_r \frac{\partial x_\alpha}{\partial r} = D_{\alpha\beta}\left[\frac{1}{r^2}\frac{\partial}{\partial r}\left(r^2 \frac{\partial x_\alpha}{\partial r}\right)\right] \tag{2}$$

where α represents the solute and β solvent. In this work, α is either the nitrogen or hydrogen gas and β is the liquid ammonia. The variations of fluid properties with temperature were also taken into account.

The radial liquid velocity of a spherical bubble can be calculated by integrating the conservation of mass equation $[\partial/\partial r(r^2 u_r) = 0]$ as follows

$$u_r = \left(\frac{R}{r}\right)^2 \frac{dR}{dt} \tag{3}$$

By assuming that the gravitational effects are negligible and the fluid is Newtonian, the momentum equation in spherical coordinates can be written as

$$\frac{\partial u_r}{\partial t} + u_r \frac{\partial u_r}{\partial r} = -\frac{1}{\rho_\beta}\frac{\partial P}{\partial r} + \frac{\mu_\beta}{\rho_\beta}\left[\frac{1}{r^2}\frac{\partial}{\partial r}\left(r^2 \frac{\partial u_r}{\partial r}\right) - \frac{2\mu_\beta}{r^2}\right] \tag{4}$$

By using the continuity equation (3) and integrating the momentum equation (4) from the bubble interface $r = R$ to $r = R_a$, the following equation can be obtained

$$R\frac{d^2R}{dt^2} + \frac{3}{2}\left(\frac{dR}{dt}\right)^2 = \frac{P(r = R) - P(r = R_a)}{\rho_\beta} \tag{5}$$

where P represents the liquid pressure. The right hand side of the Eq. (5) can be written as follows

$$\begin{aligned} P(r = R) - P(r = R_a) = {} & [P(r = R) - P_v(r = R)] + [P_v(r = R) \\ & - P_v(T_c)] + [P_v(T_c) - P_v(T_e)] + [P_v(T_e) - P(r = R_a)] \end{aligned} \tag{6}$$

The force balance across the bubble interface gives

$$P(r = R) - P_v(r = R) = -\frac{2\sigma(T_c)}{R} - \frac{4\mu_\beta}{R}\frac{dR}{dt} \tag{7}$$

Finally, by using Eqs. (6) and (7) and rearranging the terms, Eq. (5) takes the following form

$$\begin{aligned} R\frac{d^2R}{dt^2} + \frac{3}{2}\left(\frac{dR}{dt}\right)^2 = {} & \frac{P_v(T_c) - P_v(T_e)}{\rho_\beta} + \frac{R^* T_c(\sum_{\alpha=1}^2 N_\alpha)}{\rho_\beta (4/3)\pi R^3} \\ & + \frac{2\sigma(T_c)}{\rho_\beta}\left[\frac{1}{R_m} - \frac{1}{R}\right] - \frac{4\mu_\beta}{\rho_\beta R}\frac{dR}{dt} \end{aligned} \tag{8}$$

where $P_v(T_e) - P(r = R_a) = 2\sigma(T_c)/R_m$ and R_m represents the meniscus diameter of the secondary wicking due to fillets between the heat pipe wall and the artery mesh as schematically shown in Fig. 3. It is difficult to know the exact value of R_m; however, the effect of R_m on the solution is of secondary importance.

The initial and boundary conditions of the problem are as follows

$$x_\alpha(r, 0) = X_{\alpha,0} \quad \text{at } R \leqslant r \leqslant R_a \tag{9}$$

$$R(0) = R_i \quad \text{and} \quad \frac{dR}{dt}(0) = 0 \tag{10}$$

$$x_\alpha(R_a, t) = X_{\alpha,0} \tag{11}$$

$$x_\alpha(R, t) = X_{\alpha,I} \tag{12}$$

Note that the boundary condition at the bubble interface $X_{\alpha,I}$ needs to be recalculated at each time step while the bubble radius changes. The initial total solute mole fraction of the gas composition at the condenser end can be calculated from Dalton's law

$$\sum_{\alpha=1}^{2} y_\alpha = 1 - \left(\frac{P_v(T_c)}{P_v(T_e)}\right) \tag{13}$$

The mole fraction of species fy_α in the NCG is either specified or can be estimated from the Arrhenius equation for a desired life time, which will be discussed later. Then, the solute mole fraction of each component in the solution $X_{\alpha,0}$ can be calculated by using Henry's law

$$X_{\alpha,0} = \frac{fy_\alpha(\sum_{\alpha=1}^2 y_\alpha)P_v(T_e)}{k_H(T_c)} \tag{14}$$

From Raoult's law $[P_\beta = x_\beta P_v(T_c)]$, it can be assumed that the partial pressure of the solvent inside the bubble is equal to its saturation pressure at the condenser temperature since x_β inside the bubble is nearly unity. Then, for a given initial bubble radius, it is possible to calculate the total number of moles of the NCGs inside the bubble from the force balance across the bubble interface. Finally, the initial mole fraction of the solute species at the bubble external surface can be calculated from Henry's law as follows

$$x_{\alpha,I} = \frac{fx_\alpha\left(\sum_{\alpha=1}^2 N_\alpha\right)}{k_H(T_c)}\left(\frac{R^* T_c}{(4/3)\pi R^3}\right) \tag{15}$$

The mole fraction of the NCG species dissolved in the liquid fx_α is calculated by using Eq. (14).

After the mass diffusion equation is solved for a given time step using the prescribed boundary conditions, the molecular molar flux in the radial direction can be calculated by using Fick's law of binary diffusion in molar units

$$J_\alpha = -c_\beta D_{\alpha\beta}\frac{\partial x_\alpha}{\partial r} \tag{16}$$

From Eq. (16), the time rate of change of the number of moles for each component can be calculated, thus $X_{\alpha,I}$ can be updated at each time step. The details of the numerical procedure are discussed in the next section.

If a bubble formed in the condenser section is transported to the evaporator, evaporation may take place at the bubble interface. In order to study the bubble growth due to evaporation, the energy equation also needs to be taken into account

$$\frac{\partial T}{\partial t} + u_r \frac{\partial T}{\partial r} = \left(\frac{k_\beta}{\rho_\beta c_{p_\beta}}\right)\left[\frac{1}{r^2}\frac{\partial}{\partial r}\left(r^2 \frac{\partial T}{\partial r}\right)\right] \tag{17}$$

The enthalpy flux due to the diffusive flux of the solute components is neglected in Eq. (17) because this term is expected to be small. Similarly, the Soret and Dufour effects are expected to be small and also neglected. The additional initial and boundary conditions are as follows

$$T(r, 0) = T_e \tag{18}$$

$$T(R_a, t) = T_e \tag{19}$$

$$\frac{dT}{dr}(R, t) = \frac{\rho_\beta(v) h_{fg}}{k_\beta}\frac{dR}{dt} \tag{20}$$

In addition, the conservation of mass across the liquid-vapor interface needs to be satisfied, which leads to the following relation for the radial liquid velocity

$$u_r = \varepsilon\left(\frac{R}{r}\right)^2 \frac{dR}{dt} \tag{21}$$

where

$$\varepsilon = 1 - \frac{\rho_\beta(v)}{\rho_\beta(\ell)} \tag{22}$$

However, the bubble growth/collapse due to mass diffusion and phase change can be treated in two different parts because of the different time scales of these problems to simplify the solution procedure. This point will be discussed later.

The thermal properties of ammonia were calculated as a function of the temperature using the relations in [12]. Henry's constants for hydrogen–ammonia and nitrogen–ammonia binaries were taken from [13]. Diffusivity of hydrogen and nitrogen into ammonia was calculated by using Tyn–Calus method [14].

4. Numerical solution procedure

A numerical code was developed to solve the governing equations and associated boundary conditions described above by using the Galerkin finite element method. An Arbitrary Lagrangian–Eulerian method (ALE) was adopted to solve the moving boundary problem of the expanding/collapsing bubble. The momentum equation [Eq. (8)] was solved by means of the fourth-order Runge–Kutta method. The numerical solution sequence for calculating the bubble life time due to the mass diffusion was as follows:

1. To initialize the problem, solve Eq. (2) for a given initial bubble radius R with the initial interface velocity $dR/dt = 0$ and the previously described initial and boundary conditions so that the new number of moles N_α for each component is determined by using Fick's diffusion law. Then, solve Eq. (8) with the calculated values of N_α by means of the fourth-order Runge–Kutta method, which results in a new R and dR/dt.
2. Solve Eq. (2) with the new dR/dt.
3. Solve Eq. (8) with the new values of N_α and return to step 2 until the interface velocity difference between the two consecutive time steps converges to zero.
4. Calculate the mole fraction on the bubble interface $X_{\alpha,I}$ from Fick's diffusion and Henry's law equations.
5. Return to step 2 to with the new R, dR/dt and $X_{\alpha,I}$, and repeat this procedure until the bubble radius reaches 1/10th of its initial radius.

The time step required for a realistic solution was dictated by the Runge–Kutta algorithm. A typical initial time step, determined empirically, was 10^{-3} s. As the bubble collapsed, the time step was decreased gradually to 10^{-5} s. Similarly, the optimum number of nodes was determined as 100. The nodes were distributed using a logarithmic function to capture the large gradients near the bubble interface.

For the bubble growth due to the evaporation, the numerical solution sequence was similar to the mass diffusion one as described above. The solutions were obtained for an assumed evaporator superheat. The bubble growth was then initiated in a superheated liquid and the momentum equation was solved to calculate the new R and dR/dt. This allows the calculation of the heat flux at the interface, Eq. (20). Later, the thermal diffusion equation [Eq. (17)] was solved to produce a new interface temperature. The sequence between the momentum and thermal diffusion equations was iterated until convergence on dR/dt at a given time step. This procedure was repeated until the artery was blocked by the growing bubble.

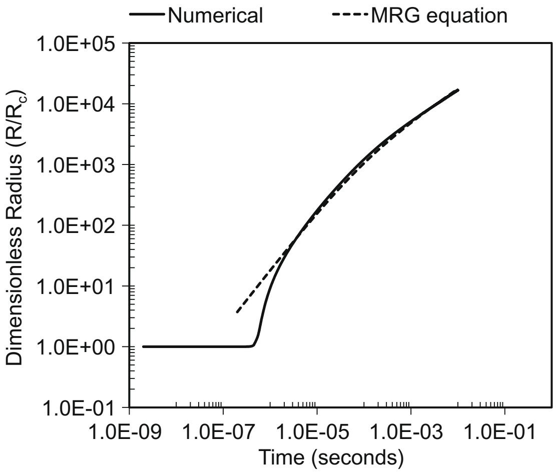

Fig. 4. Comparison of the numerical results of bubble growth with the analytical solution of MRG equation [15].

The validity of the numerical model was tested against the well-studied bubble growth problem in a superheated liquid. This problem is very similar to the above problem with an additional complexity due to the sudden bubble growth from a critical size. For this particular problem, the momentum equation takes the following form

$$R\frac{d^2R}{dt^2} + \frac{3}{2}\left(\frac{dR}{dt}\right)^2 = \frac{P_v(T) - P_\infty}{\varepsilon\rho_\beta} - \frac{2\sigma(T)}{\varepsilon\rho_\beta R} - \frac{4\mu_\beta}{\varepsilon\rho_\beta R}\frac{dR}{dt} \tag{23}$$

The initial bubble critical size was calculated from the pressure balance across the liquid–vapor interface [$R_c = 2\sigma(T)/(P_v(T) - P_\infty)$]. To initiate the growth process, an initial small disturbance was required. In [15], it was shown that this disturbance only affects the growth in the early stages but not the subsequent bubble growth. The numerical results were obtained for water at atmospheric pressure with a superheat of 40 °C and $R_c = 0.527$ mm. Fig. 4 shows a comparison of the calculated results and analytical solution given by Mikic et al. [16]. The bubble radius was nondimensionalized with the critical radius R_c. The agreement was very good with a similar success reported in [15]. The discrepancy in the very early stages of the growth, which is clearly visible on a log–log scale in Fig. 4, is mainly due to the neglecting the surface tension effects in the analytical solution.

5. Results and discussion

The main characteristics of the heat pipes used in this work are given in Table 1. Both of the heat pipes used ammonia as working fluid and they were made of stainless steel. In addition, the VCAHP had a gas reservoir of 100 m^3 and contained 1.6 g of nitrogen as the control gas. The heat pipes were instrumented with T-type

Table 1
Main characteristics of the heat pipes.

Main characteristics	Type of heat pipe	
	VCAHP	CCAHP
Outer diameter (mm)	12.2	12.2
Total length (mm)	2065.0	1295.0
Length of evaporator (mm)	141.0	280.0
Length of condenser (mm)	700.0	280.0
Working fluid mass (g)	25.0	15.0

thermocouples attached to their outer wall. Heat was applied by electric heaters and cooling was provided by a nitrogen shroud located around a thermal vacuum chamber for the VCAHP and a recirculating chiller for the CCAHP. More detailed description of the test setup and the main thermal performance characteristics can be found in [17] and [18]. Therefore, only some typical and relevant experimental results are presented in this paper.

The NCG generation in the heat pipes was estimated for a conservative life time of 20 years by using the Arrhenius equation [$k_0 \exp(-E_A/RT)$]. The constants in this equation were taken from a recent experimental work [19], where $k_0 = 2.3 \times 10^{-2}\ 1\ \mathrm{s}^{-1}$ and $E_A = 7000\ \mathrm{J\ mol}^{-1}$. The total mass of NCG generated in the VCAHP was calculated as 1.75×10^{-3} g with 1.55×10^{-4} mol of H_2 and 5.16×10^{-5} mol of N_2. Considering that the ammonia decomposition will occur according to the reaction: $2NH_3 \rightarrow N_2 + 3H_2$, and taking into account that 1.6 g nitrogen injected into the heat pipe as control gas, the nitrogen and hydrogen molar fractions were calculated as 99.73% and 0.27%, respectively. The similar calculations for the CCAHP resulted in a total NCG mass of 1.05×10^{-3} g with 9.29×10^{-5} mol of H_2 and 3.10×10^{-5} mol of N_2.

The bubbles generated in the condenser section were analyzed first. The bubbles in the condenser can appear as a result of one of the mechanisms discussed above. The lifetimes of such bubbles were calculated for three different initial bubble radii: 100, 200, 400 μm and the results obtained for the VCAHP with $T_e = 273$ K and $T_c = 269$ K are shown in Fig. 5. In this figure, the bubble life time is the time at which the bubble radius reaches 1/10th of its initial radius and the bubble radius is nondimensionalized with the initial bubble radius. The 100 μm bubble was reabsorbed in 13.6 s. The time of reabsorption increased with the bubble size, 84.1 s for the 200 μm and 488.7 s for the 400 μm bubbles. This increase was mainly due to the increasing volume-to-area ratio with increasing radius.

The bubble collapse times for the CCAHP showed a similar trend. The results were 9.9, 70.8 and 446.6 s for the three respective initial bubble radii with $T_e = 304$ K and $T_c = 300$ K. The difference in bubble collapse times between the VCAHP and CCAHP was both due to the different NCG fraction and different operating temperatures. When the CCAHP bubble collapse times were calculated with the same operating temperatures as the VCAHP, it took longer for the bubbles to collapse: 14.1, 86.2, and 496.1 s, respectively. This was because of the decreased solubility and diffusivity of the hydrogen and nitrogen with the decreasing temperature. The bubble life time for the CCAHP was slightly longer since the hydrogen is approximately 1.35 times less soluble than the nitrogen at this temperature range although the hydrogen is 1.4 times more diffusive. These results suggest that the bubbles in a heat pipe prior to startup can be eliminated by keeping the pipe at high temperatures for an extended period.

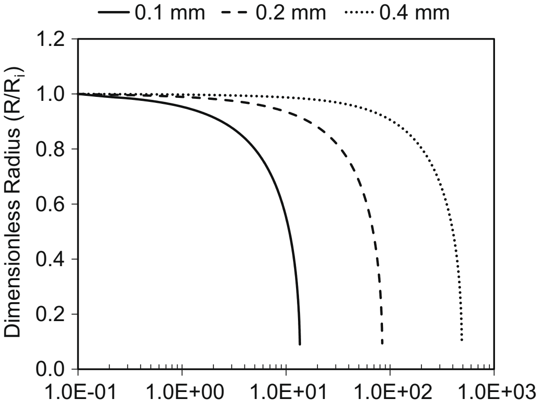

Fig. 5. Bubble life time for three different initial bubble radii.

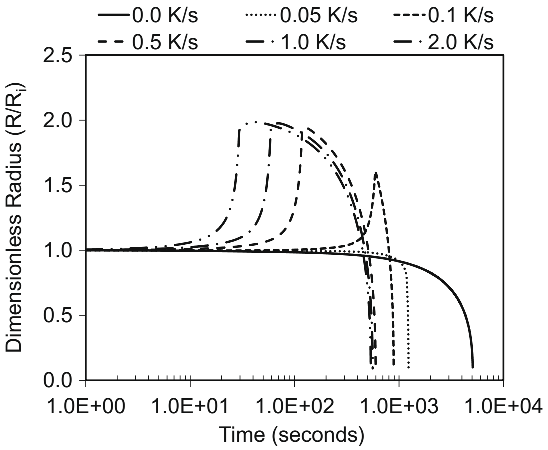

Fig. 6. Bubble life time under different warm-up rates for $R_i = 200$ μm.

In [10], the bubble collapse times were studied while thawing of a frozen condenser at a prescribed warm-up rate. The bubble collapse time as large as 64,411 s was reported for a 200 μm bubble in a helium/methanol mixture. For the CTS pipes with 90% N_2 and 10% He in methanol, the collapse time was 10,777 s. Considering a similar frozen condenser scenario, the bubble collapse times were calculated assuming that the condenser was thawed to 210 K after being frozen. Then, the condenser was allowed to reach its normal operating temperature with a prescribed warm-up rate: $T_c = 273$ K for the VCAHP and 300 K for the CCAHP. Fig. 6 shows the results obtained for the VCAHP for an initial bubble radius of 200 μm. The bubble collapse times quickly decreased with increasing warm-up rates. At a certain warm-up rate, the bubble first started to grow and then collapsed at a fast rate, see warm-up rates 0.1 K s^{-1} and higher in Fig. 6. At higher warm-up rates, the bubble growth started earlier. Not surprisingly, the bubble collapse times did not change significantly since the condenser reached its operating temperature quickly at higher warm-up rates. More importantly, the bubble growth was limited to approximately twice the initial radius without causing an artery blockage. Similarly, for an initial radius of 400 μm and a warm-up rate of 4 K s^{-1}, the bubbles did not grow more than twice the initial radius. Limiting the condenser warm-up rates for large radius bubbles will clearly be desirable to avoid a potential condenser blockage. At the same time, the bubbles collapsed much faster at high warm-up rates. Thus, there is an optimum warm-up rate for a given bubble initial radius. In any event, avoidance of freezing is needed to avoid risk of condenser artery blockage as it was also recommended in [10].

A comparison of the bubble collapse times for both heat pipes starting from a bubble initial radius of 200 μm as a function of warm-up rates are shown in Table 2. The evaporator temperatures were 269 K for VCAHP and 304 K for CCAHP. All the bubble collapse times listed in Table 2 were higher than the previous values obtained for the normal operating temperatures as a result of

Table 2
A comparison of the bubble collapse times as a function of warm-up rates.

Type of heat pipe	Warm-up rate (K/s)					
	0.0	0.05	0.1	0.5	1.0	2.0
Bubble collapse time (s)						
VCAHP	5078.5	1233.8	887.7	596.4	559.3	536.1
CCAHP	24,268.0	1888.1	1322.9	840.6	781.7	753.2

decreasing solubility and diffusivity of hydrogen and nitrogen with decreasing temperature. The bubble collapse time for the CCAHP at a low condenser temperature (without condenser warm-up) was remarkably high since the hydrogen solubility dropped very quickly at low temperatures and reached a very low value (4.85×10^{-6} 1 atm^{-1}) at 210 K. This delayed the reabsorption of the bubble and its effect was more pronounced for the CCAHP because of the higher hydrogen mole fraction inside the bubble.

The collapse times for the CCAHP were longer than those for the VCAHP for all cases studied. This was again due to the strong dependence of the hydrogen solubility on the temperature. From 300 to 210 K, the hydrogen solubility decreased 16.2 times, whereas the nitrogen solubility decrease was 10.2 times. This resulted in a N_2/H_2 solubility ratio variation from 2.5 at 210 K to 1.6 at 300 K. Obviously, the CCAHP was most affected by these variations due to the higher hydrogen mole fraction.

Following the study of bubbles in the condenser section, the bubble life time in the evaporator section was studied. The bubble formed in the condenser or adiabatic section can be carried towards the evaporator by condensate flow [20]. Considering that the subcooled condensate normally reaches the evaporator as saturated liquid [21] due to the heat transfer from the vapor flow in the adiabatic section and pressure drop in the artery, the arterial liquid will be superheated in the heat input region, leading to the growth of the transported bubbles. Alternatively, boiling can be initiated in the evaporator region in the microcavities of the artery wall. The bubble growth rate as a function of the superheat was calculated and the results are shown in Fig. 7. The superheat in the evaporator is very difficult to measure and no measurements were reported in the literature. The incipient superheat has a stochastic nature and depends in a complicated way on many factors including presence of NCG, surface and fluid properties. As a result, a range of superheats from 1 to 6 K was studied. For these calculations, a bubble initial radius of 200 μm was considered and the calculations were run until the bubble reached a radius of 1 mm. The bubble diameters were nondimensionalized by the artery radius. Not surprisingly, the bubble growth rate increased with the superheat. For comparison, the bubble growth time to reach the artery hydraulic radius was 2.99, 0.75, 0.19 and 0.08 s, respectively for the superheats studied (1, 2, 4 and 6 K). In the evaporator, higher superheats are of course possible. In this case, the bubble will grow and block the artery almost instantaneously. These results clearly show that the artery blockage is almost unavoidable if a bubble reaches the evaporator section. Therefore, it is hardly possible for the heat pipes with the presented artery design to operate without the help of the menisci coalescence method. It should be noted that the venting pores will result in an increase in the pressure drop; therefore, the pores were limited to the most critical evaporator section.

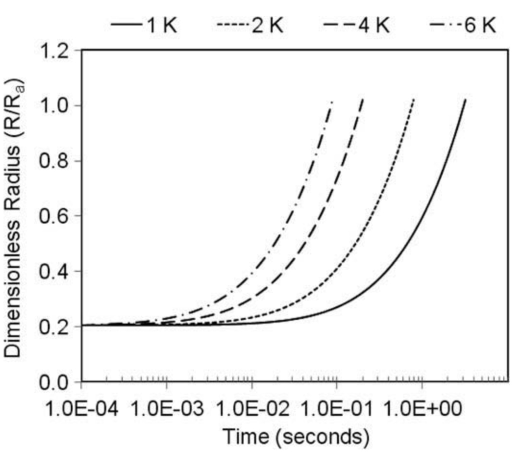

Fig. 7. Bubble growth time in the evaporator under different superheat values for $R_i = 200$ μm.

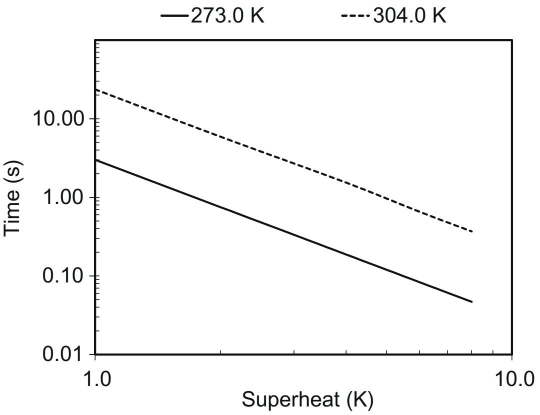

Fig. 8. Time required to block the artery as a function of liquid superheat at two different operating temperatures.

In [22], the bubble migration due to thermocapillary flow in the surface of a bubble was studied. It was suggested that the bubble mobility can be increased by introducing a small amount of inert gas especially in low gravity environment. Based on this work, it can be speculated that the control gas in a VCAHP could be beneficial in helping bubbles move towards to the evaporator and thus decreasing the potential artery blockage risk for space applications.

The results obtained for the CCAHP followed the same trend since the growth times were dominated by the phase change of ammonia and the influence of the NCG composition inside the bubble on the results was secondary. Since the CCAHP was tested at a higher operating temperature, the bubble growth times were different. Fig. 8 shows the time required to block the artery as a function of liquid superheat calculated at the operating temperature of 304 K for the CCAHP and 273 K for the VCAHP. Note that the growth time almost linearly decreased with the superheat on a log–log scale. The time required to block the artery was increased approximately 7.8 times when the operating temperature was increased 1.11 times.

One remaining question is whether the NCG-supported bubbles generated in the condenser will grow while being convected towards the evaporator, either because of the gas insertion into the bubble or coalescence of the smaller bubbles to form large elongated bubbles, eventually blocking the artery. The experimental work carried out in [10] indicated that the bubble merging mechanism was statistical. In another experimental work [9], it was observed in glass systems that the arterial bubbles were statistically to be more elongated than spherical. The spherical bubble model presented in this work cannot be used to analyze the merging of bubbles immersed in an arterial flow. Saaski [20] studied the dynamic stability of sausage-shaped arterial gas occlusions by considering a fully developed laminar pipe flow along with a steady-state occlusion of given length to propose a simplified criterion for the occlusion growth. It was found that the elongated bubbles may require days to dissolve back into the working fluid. At the same time, low arterial flow can significantly contribute to gas dissolution and shorten bubble life time.

For our design, as a worst case scenario, the elongated bubbles formed by merging of small bubbles may block the arterial flow, resulting in an evaporator dry out. Then, they should continue to grow until they reach the evaporator. Once an elongated bubble reaches the evaporator, it will be vented through the venting pores, leading to priming of the artery. Since the mathematical model cannot directly validate this scenario, the heat pipes were

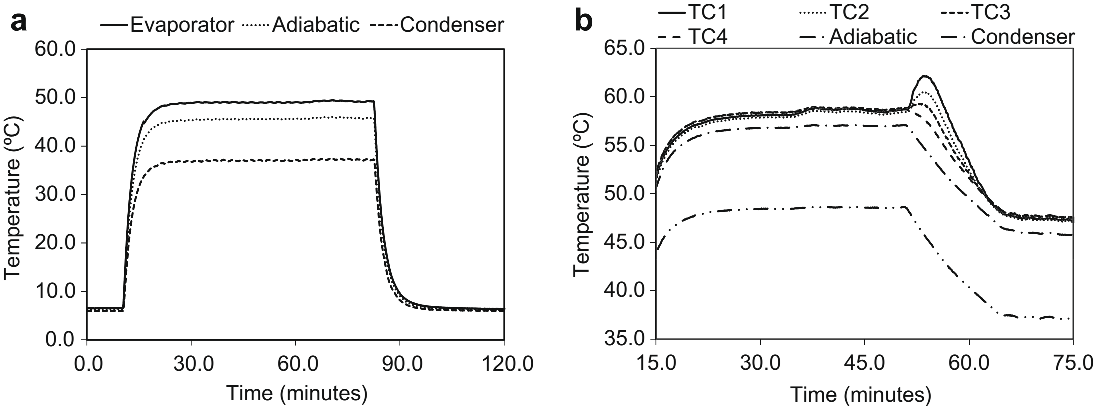

Fig. 9. Temperature profiles (a) for the rapid startup test (from 0 to 300 W) (b) for rapid cooldown test (from 293 to 278 K).

tested at various adverse conditions to investigate arterial blockage possibility. Two typical experimental results obtained by applying a large startup power up to 95% of maximum load and rapid condenser cooldown tests for the CCAHP are presented in Fig. 9(a) and (b), respectively. For the rapid startup test, the heat load was increased instantaneously from 0 to 300 W. In Fig. 9(a), the thermocouples located in the middle of the evaporator, adiabatic and condenser sections were shown. During this test and similar large step startup tests, there was no indication of arterial blockage. In Fig. 9(b), when the heat pipe was at equilibrium under a heat load of 300 W and a sink temperature of 293 K, the sink temperature was suddenly dropped to 278 K. The first four evaporator thermocouples, (The first one was 5 mm away from the evaporator end and the others were subsequently located at 10 mm intervals.) and the thermocouples in the middle of the adiabatic and condenser sections are shown. The evaporator thermocouples responded approximately 30 s later than the first drop observed in the condenser thermocouples. The first three evaporator thermocouples rose temporarily and then dropped to the level of other evaporator thermocouples. This behavior suggested sudden boiling in the small region closest to the evaporator end. Then, the bubbles vented through the venting holes and artery was rewetted. However, the heat pipe did not experience a full deprime as evidenced from the other evaporator thermocouples. It should also be noted that the same test was repeated five times and the temperature rise of the first there thermocouples was random. In two cases, there was no increase. The result presented in Fig. 9(b) was the largest temperature overshoot observed. The random nature of bubble formation is not surprising because of the statistical nature of nucleation.

The startups were also performed at an adverse elevation (evaporator over condenser) to help moving the NCGs towards the evaporator prior to a startup. No sign of arterial blockage was observed at elevations up to 3.2 mm. However, the arterial heat pipes were found to be very sensitive to the adverse elevation. The static capillary limit of this artery was estimated to be about 6.3 mm and the pipe performance dropped quickly when the elevation approached to this value.

In [11], for the tapered artery heat pipe design, it was found that longer heat pipes (9144 mm) showed random pipe failures following a freeze/thaw cycle whereas tests with shorter pipes (3048 mm) under the same conditions did not result in a failure of the heat pipe. This was attributed to the longer bubble travel times in longer heat pipes, providing sufficient time for bubble coalescence. Although the heat pipe in [11] has a very different design, caution is necessary in general for very long heat pipes. It should also be added that deprime in [11] was observed when the bubble entered the artery of the evaporator which was identified by the calculated bubble transport time. Based on this observation, the venting holes in our pipes should be able to vent large bubbles as it was discussed previously, allowing the use of longer pipes. More testing is required to demonstrate the robustness of the arterial design under other unfavorable conditions.

Finally, a discussion on the relations used for Henry's constant and diffusion coefficients are necessary. In [13], the relations for Henry's constant were confirmed with the earlier experimental works and shown to be better than the earlier correlations. However, the relations for diffusion coefficients were more uncertain. We compared several diffusion correlations published. The difference between some correlations was up to 30%. Tyn–Calus [14] correlation was chosen because of the lower error reported and closer match to the fluids studied in this work. It was shown that different diffusion correlations can influence the bubble collapse time up to 20% by using extreme values. However, this uncertainty in diffusion coefficients does not influence the general trend presented or conclusions.

6. Conclusions

The NCG-supported bubbles in a VCAHP and CCAHP using a unique artery design were studied. Some past AHP designs were reviewed and the failures induced due to the NCG-supported bubbles in these pipes and proposed solutions were discussed. The one-dimensional time-dependent mass diffusion, momentum and energy equations in spherical coordinates were solved by the FEM. To tackle the moving boundary problem of bubble interface, an ALE method was implemented into the FEM solver. The numerical method was validated by the well-known homogeneous bubble nucleation problem. The resulting equations were solved for two different scenarios: the first scenario involves mass diffusion of NCG molecules back to the working fluid in the condenser and the second one is governed by the evaporation on the bubble interface in the evaporator. These two problems were solved separately since the dissolution of the NCGs into the working fluid was found to be much slower than the bubble growth due to the evaporation of the fluid into the bubble.

The NCG-supported bubbles in the condenser were collapsed relatively fast at the expected normal operating temperatures. The reabsorption time increased quickly at low temperatures and this was governed mostly by the quickly decreasing solubility of hydrogen with temperature. If the condenser is frozen during a mission, it seems that there is an optimum warm-up rate to accelerate the bubble collapse without causing an artery blockage. If the bubbles were carried to the evaporator, it was shown that they expanded very quickly because of the superheated liquid in the heated region. However, the blocked evaporator artery, either due to the growing bubbles in the evaporator or an elongated bubble formed by merging of smaller bubbles reaching the evaporator, will prime quickly because of the venting pores on the arterial mesh. The experimental results under unfavorable conditions, including rapid startup, condenser cooldown and adverse elevation demonstrated the robustness of the arterial design and its rapid self-priming capability.

Acknowledgements

The support from Natural Sciences and Engineering Research Council of Canada under Discovery Grants Program is greatly appreciated. The author would also like to thank David Antoniuk for helpful discussions and Konstantin Goncharov for providing the test articles.

References

[1] R.S. Gaugler, U.S. Patent No. 2350348, 1944.

[2] G.M. Grover, T.P. Cotter, G.F. Ericson, Structures of very high thermal conductivity, J. Appl. Phys. 35 (1964) 1190–1191.

[3] K.A. Goncharov, A.A. Orlov, V.A. Kolesnikov, A.A. Kochetkov, Arterial heat pipes in Russian spacecraft, in: Proc. of the IV Minsk Int. Seminar in Heat pipes, Heat Pumps, Refrigerators, 2000.

[4] I.M. Blinchevskii, B.F. Aptekar, Y.M. Baum, Prom. Teplotekh. 5 (6) (1983) 26–29 (in Russian).

[5] J.E. Eninger, Menisci coalescence as a mechanism for venting noncondensable gas from heat-pipe arteries, AIAA-1974-748, 1974.

[6] D.J. Wanous, B.D. Marcus, J.P. Kirkpatrick, A variable conductance heat pipe flight experiment: performance in space, AIAA-1975-725, 1975.

[7] P.R. Mock, D.B. Marcus, E.A. Edelman, Communications Technology Satellite: a variable conductance heat pipe application, J. Spacecraft Rockets 12 (12) (1975) 750–753.

[8] R. Schlitt, Evolution of heat pipe technology for satellite application, in: Proc. of the 10th Int. Heat Pipe Conf., 1997.

[9] E.W. Saaski, Investigation of bubbles in arterial heat pipes, NASA-CR-114531, 1972.

[10] D. Antoniuk, D.K. Edwards, Depriming of arterial heat pipes: an investigation of CTS thermal excursions, NASA-CR-165153, 1980.

[11] H.R. Holmes, A.R. Field, The gas-tolerant high-capacity tapered artery heat pipe, AIAA-1986-1343, 1986.

[12] P.J. Brennan, E.J. Kroliczek, Heat Pipe Design Handbook, NASA NAS5-32406, Maryland, 1979, pp. 62–67.

[13] M.R. Sawant, A.W. Patwardhan, V.G. Gaikar, M. Bhaskaran, Phase equilibria analysis of the binary N_2–NH_3 and H_2–NH_3 systems and prediction of ternary phase equilibria, Fluid Phase Equilib. 239 (2006) 52–62.

[14] M.T. Tyn, W.F. Calus, Temperature and concentration dependence of mutual diffusion coefficients of some binary liquid systems, J. Chem. Eng. Data 20 (3) (1975) 310–316.

[15] H.S. Lee, H. Merte, Spherical vapor bubble growth in uniformly superheated liquids, Int. J. Heat Mass Transfer 39 (12) (1996) 2427–2447.

[16] B.B. Mikic, W.M. Rohsenow, P. Griffith, On bubble growth rates, Int. J. Heat Mass Transfer 13 (4) (1970) 657–666.

[17] K.A. Goncharov, O.A. Golovin, J.V. Panin, K.V. Korzhov, et al. Arterial variable conductive heat pipe, in: Proc. of the 14th Int. Heat Pipe Conf., 2007.

[18] T. Kaya, M. Garcia, Comparative investigation of operational performance characteristics of axially grooved and arterial heat pipes, Heat Mass Transfer 43 (8) (2008) 739–750.

[19] A.L. Luks, A.G. Matveev, High-efficient ammonia heat-pipes within energy-efficient systems for temperature control of large dimension constructions of spacecraft (in Russian), Nat. Sci. Ser. Tech. Eng. Syst.Vestnik of Samara State University 6 (56) (2007) 401–418.

[20] E.W. Saaski, Arterial gas occlusions in operating heat pipes, AIAA-1975-657, 1975.

[21] B.D. Marcus, Theory and design of variable conductance heat pipes, NASA-CR-2018, 1972.

[22] J.M. Papazian, R.L. Kosson, Effect of internal heat transport on the thermal migration of bubbles, AIAA J. 17 (11) (1979) 1279–1280.